



# Damping and mode shape modification for additively manufactured walls with captured powder

Tony Schmitz<sup>a,b,\*</sup>, Michael Gomez<sup>a,b</sup>, Barrett Ray<sup>a</sup>, Eric Heikkinen<sup>a</sup>, Kevin Sisco<sup>a</sup>,  
Michael Haines<sup>a</sup>, Jessica S. Osborne<sup>c</sup>

<sup>a</sup> University of Tennessee, Knoxville, 1512 Middle Dr., Knoxville, TN, 37996, USA

<sup>b</sup> Energy and Transportation Science Division, Oak Ridge National Laboratory, Oak Ridge, TN, 37830, USA

<sup>c</sup> Integrated Operations Support Division, Oak Ridge National Laboratory, Oak Ridge, TN, 37830, USA

## ARTICLE INFO

### Keywords:

Additive manufacturing  
Powder  
Metal  
Damping  
Mode shape  
Structural dynamics

## ABSTRACT

This paper describes the fabrication, modeling, and dynamic testing of laser powder bed fusion stainless steel walls with captured powder cores. The purpose of the study is to determine the increased structural damping, or energy dissipation, and mode shape modification caused by the inclusion of the unmelted powder core within the solid walls. It is shown experimentally that the damping increases with larger powder core width and that the damping addition is mode dependent. Damping increases over the solid wall values by factors of 2.9–225 are reported depending on the mode number and core width. It is also seen that the mode shapes are distorted relative to the solid wall results as the core width is increased and wall thickness is decreased. Comparisons with finite element models confirm this trend.

## 1. Introduction

It is generally accepted that additive manufacturing (AM) enables new design freedom, complex structures, mass customization, waste minimization, and fast prototyping. These design and fabrication capabilities are being adopted in many industries from biomedical to aerospace to buildings and protective structures [1–4]. A subset of the AM ecosystem, metal additive, can be categorized by the powder or wire feedstock material [5,6]. Powder-based technologies include powder feed (or blown powder) and powder bed fusion (PBF). In this paper, the opportunity to increase structural damping and modify the corresponding mode shapes for PBF metal components is demonstrated. This research builds on the recent efforts presented in Ref. [7], where PBF aluminum cylinders with different volumes of captured powder were impact tested using free-free boundary conditions and the solid damping factor was extracted from measured frequency response functions. A significant increase in damping was demonstrated with increased captured powder volume for the same cylinder external geometry

(diameter and length), but different wall thicknesses.<sup>1</sup>

To identify the structural dynamics of AM components, the principles of modal analysis may be applied. This includes the measurement or analytical/numerical modeling of eigenvalues (or natural frequencies) and eigenvectors (or mode shapes) that define the vibration behavior. For spatial positions on a selected structure (with corresponding boundary conditions), the frequency response function, or FRF, can be measured or predicted and the natural frequency, modal stiffness, and modal damping ratio can be extracted for each mode [8]. In most instances, the design intent is to maximize the stiffness and damping; this reduces the vibration magnitude due to external dynamic forces or moments.

In this research, metal powder is intentionally retained inside PBF stainless steel walls with clamped-free-free-free (CFFF) boundary conditions. The intent is to achieve increased damping and mode shape modification, where the internal, captured powder serves as an energy dissipation mechanism during vibration of the surrounding solid wall. This work builds on seminal research by Scott-Emuakpor et al. [9–13].

\* Corresponding author. University of Tennessee, Knoxville, 1512 Middle Dr., Knoxville, TN, 37996, USA.

E-mail addresses: [tony.schmitz@utk.edu](mailto:tony.schmitz@utk.edu) (T. Schmitz), [gomezmg@ornl.gov](mailto:gomezmg@ornl.gov) (M. Gomez), [bray15@vols.utk.edu](mailto:bray15@vols.utk.edu) (B. Ray), [ehikken@vols.utk.edu](mailto:ehikken@vols.utk.edu) (E. Heikkinen), [ksisco@vols.utk.edu](mailto:ksisco@vols.utk.edu) (K. Sisco), [mhaines2@vols.utk.edu](mailto:mhaines2@vols.utk.edu) (M. Haines), [osbornejs@ornl.gov](mailto:osbornejs@ornl.gov) (J.S. Osborne).

<sup>1</sup> Notice: This manuscript has been authored by UT-Battelle, LLC, under contract DE-AC05-00OR22725 with the US Department of Energy (DOE). The US government retains and the publisher, by accepting the article for publication, acknowledges that the US government retains a nonexclusive, paid-up, irrevocable, worldwide license to publish or reproduce the published form of this manuscript, or allow others to do so, for US government purposes. DOE will provide public access to these results of federally sponsored research in accordance with the DOE Public Access Plan (<http://energy.gov/downloads/doe-public-access-plan>).

**Table 1**  
Laser PBF processing parameters.

Value				
Laser power (W)	Scan velocity (mm/s)	Hatch size (μm)	Laser spot size (μm)	Preheat temperature (deg C)
300	1000	90	90	100

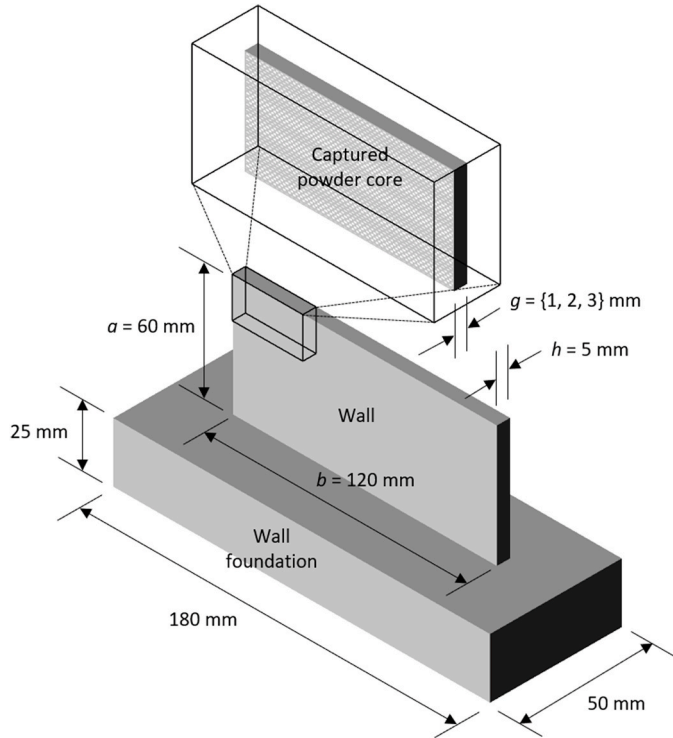


**Fig. 1.** Design geometry for CFFF walls and foundation. The inset shows the captured (unmelted) powder core centered within the wall.

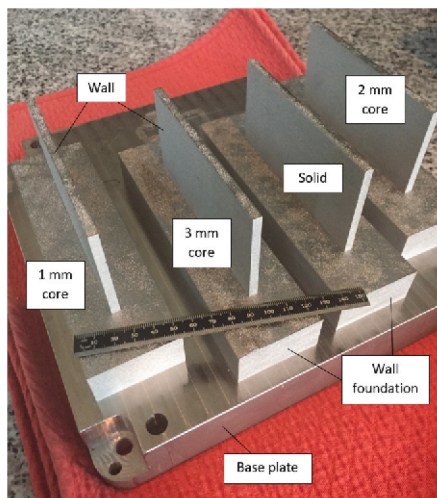


**Fig. 2.** Photograph of four stainless steel walls printed on a single base plate. From left to right, the geometries are: 1 mm captured powder core, 3 mm core, solid, and 2 mm core. A 152 mm ruler is included to provide scale.

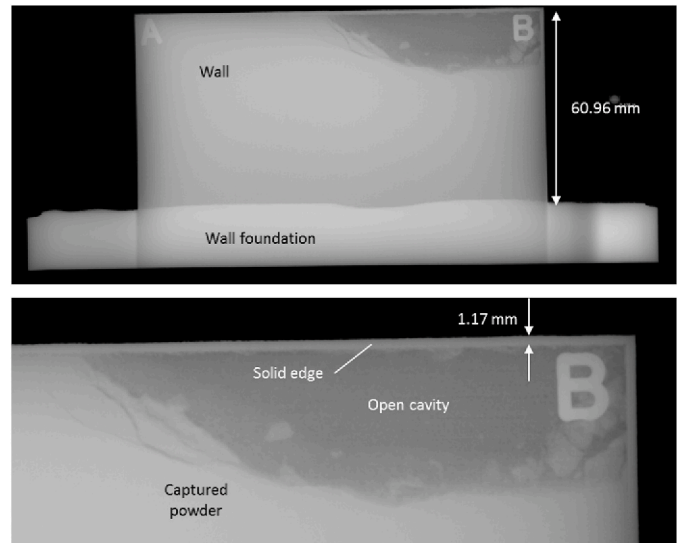


**Fig. 3.** CT scan for wall with 3 mm powder core. (Top) Entire wall and foundation. (Bottom) Enlarged view of open cavity with captured powder.

This group first used laser PBF to produce components that contain internal geometries with trapped powder. Their application domain is integrally bladed rotors, where the monolithic designs do not offer the airfoil-to-disk frictional energy dissipation obtained for assembled designs. They studied damping for high strain and long duration tests and evaluated the endurance, repeatability, and recovery of the damping provided by the unmelted powder pockets in beam geometries. This research also complements previous particle damper research, where

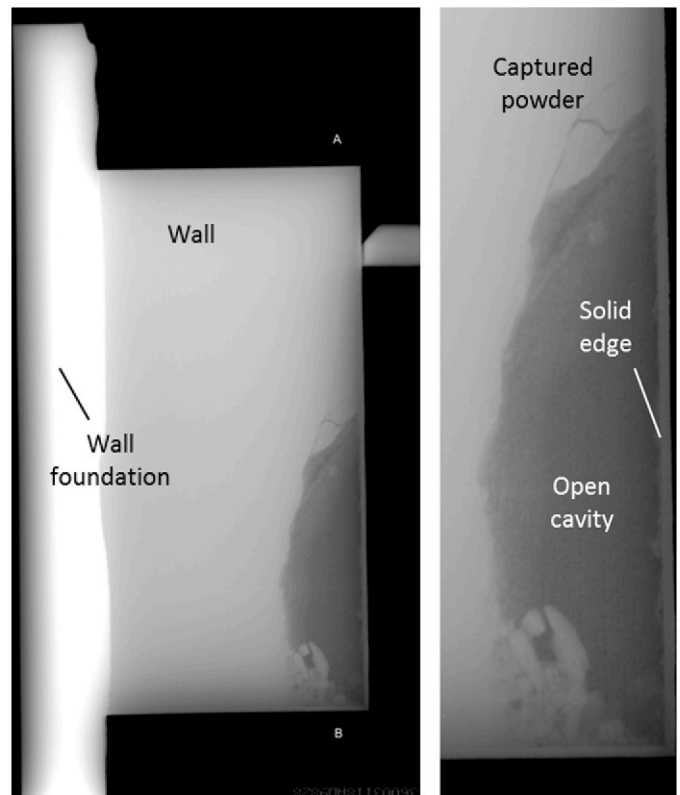


**Fig. 4.** CT scan for wall with 3 mm powder core after 90 deg rotation. (Top) Entire wall and foundation. (Bottom) Enlarged view of open cavity with captured powder. It is seen that the powder near the open cavity edge was repositioned by the rotation.

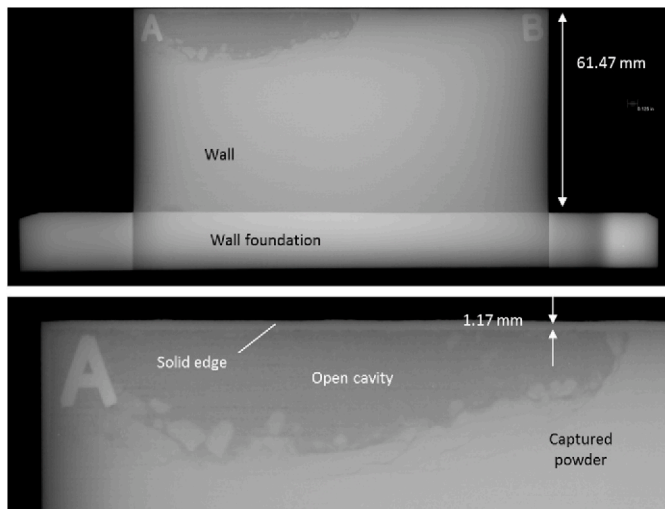


**Fig. 5.** CT scan for wall with 2 mm powder core. (Top) Entire wall and foundation. (Bottom) Enlarged view of open cavity with captured powder. The cavity location is different, but is qualitatively the same as the 3 mm core (Figs. 3 and 4).

energy is dissipated by a moving particle bed (e.g., sand in a box) through collisions between the particles and container walls and collisions, sliding friction, and rolling friction between the particles [14].

## 2. Experimental procedure

The CFFF walls for this study were printed using a Farsoon FS271 M to carry out laser PBF with a 500 W Yb fiber laser and 271 mm × 271 mm × 340 mm build volume. In the laser PBF process, a laser melts powder layer-by-layer to form parts with relative densities up to 99.9% [15]. Laser PBF parts in the as-built condition typically exhibit higher strength, but less elongation, at failure than traditional wrought or cast alloys of the same composition due to large residual stress and high dislocation density [16,17]. The walls were made from 316L stainless steel spherical powder with a 15 μm–45 μm size range; this range was provided by the manufacturer and is standard for laser PBF [18,19]. The range comes from two sorting steps. First, a mesh size of 45 μm is used to exclude particles larger than this value. Second, a mesh size of 15 μm is used to exclude particles smaller than this value. It does not define the distribution of particle sizes. The walls were printed using a raster-in-stripes scan strategy with a 10 mm stripe width. The layer height was held constant at 40 μm throughout the build. The processing parameters are listed in Table 1.

The nominal wall geometry is provided in Fig. 1, where the wall foundation was included in the design to enable the clamped boundary condition to be part of the PBF build, rather than relying on the first few build layers at the base plate-wall interface to establish the ideally rigid boundary. Due to large thermal gradients, these layers do not typically provide a microstructure or porosity level that is consistent with the remainder of the build. Therefore, a good approximation of the clamped boundary condition could not be ensured with this strategy.

Both solid and powder filled designs were defined, where the external dimensions,  $a$ ,  $b$ , and  $h$ , shown in Fig. 1 were unchanged. For the powder filled designs, the internal (unmelted) cores with  $g = \{1, 2, \text{ and } 3\}$  mm widths were centered within the 5 mm wall width. In all cases, the wall top, edges, and bottom were solidified during the vertical wall print so that the powder filled core was entirely captured within the build volume. The commanded distance from the core edges to the wall top, sides, and bottom was 1 mm. A photograph of the four printed walls is displayed in Fig. 2.

To better understand the as-built geometry, computed tomography (CT) scans were completed. Fig. 3 displays results for the 3 mm powder

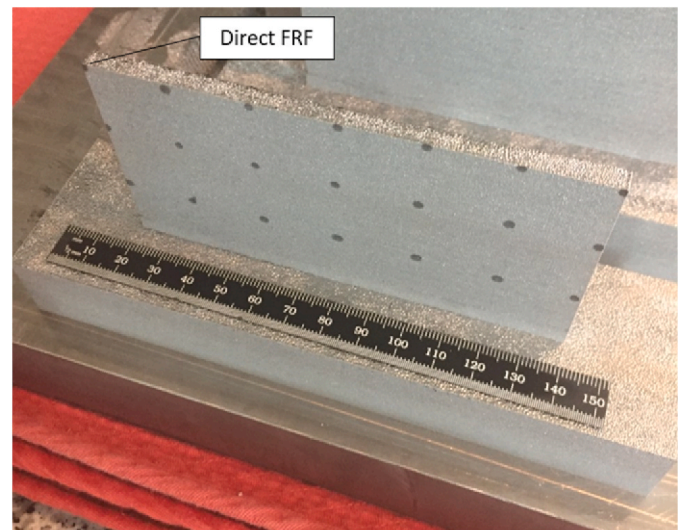


**Fig. 6.** Impact testing setup for FRF measurements. The direct FRF location is identified; all other locations represent cross FRFs. The build plate was placed on a soft support to avoid potential dynamic interactions with the table. The support was composed of three quilted cloth pads with a compressed thickness of 5 mm.

core. It is observed that the unmelted powder did not completely fill the internal volume after cooling and settling. The character of the powder near the edge of the open cavity shows that the powder is free to move. To confirm this behavior, the same part was rotated 90 deg in the clockwise direction and the CT scan was repeated. It is observed in Fig. 4 that the powder near the open cavity edge was repositioned, but the open cavity maintained a similar location. Fig. 5 shows the 2 mm powder core scan. The results are similar.

Impact testing for all four walls was completed using a small hammer (PCB model 086E80), low-mass accelerometer (PCB model 352C23), and MLI's MetalMax TXF software. Tests were completed over a grid of points spaced at 20 mm intervals in the horizontal and vertical directions; see Fig. 6. A direct FRF, where the force input is applied and the accelerometer output is recorded at the same spatial location, was completed at the top left corner. For the cross FRFs, the accelerometer position was constant (top left, back side), but the impact force was applied at the 20 remaining grid locations (21 total measurements for the 3 × 7 grid). The direct FRF for each wall was used to identify the natural frequency and dimensionless viscous damping ratio for the first three modes. The combination of direct and cross FRFs for each wall were used to define the corresponding three mode shapes (or dynamic deformation pattern at the selected natural frequency) [8]. Each FRF was composed of 8–12 impacts, where the results from each impact were averaged in the frequency domain to determine the final direct or cross FRF.

An example FRF measurement result is shown in Fig. 7. The direct FRF for the solid wall is displayed using linear (left) and semi-logarithmic (right) formats due to the significant change in magnitudes between the first three modes. For the semi-logarithmic plot, both the resonant (local maxima) and anti-resonant (local minima) frequencies are observed. It is also seen that the solid wall is lowly damped based on the sharp peaks.

## 3. Finite element modeling

The wall dimensions were selected to: 1) capture the first three modes within the measurement bandwidth (approximately 5 kHz); and 2) provide sufficient wall width for inclusion of the captured (unmelted) powder cores. Finite element models of the CFFF walls were produced in SOLIDWORKS, where the powder core was included using an extruded

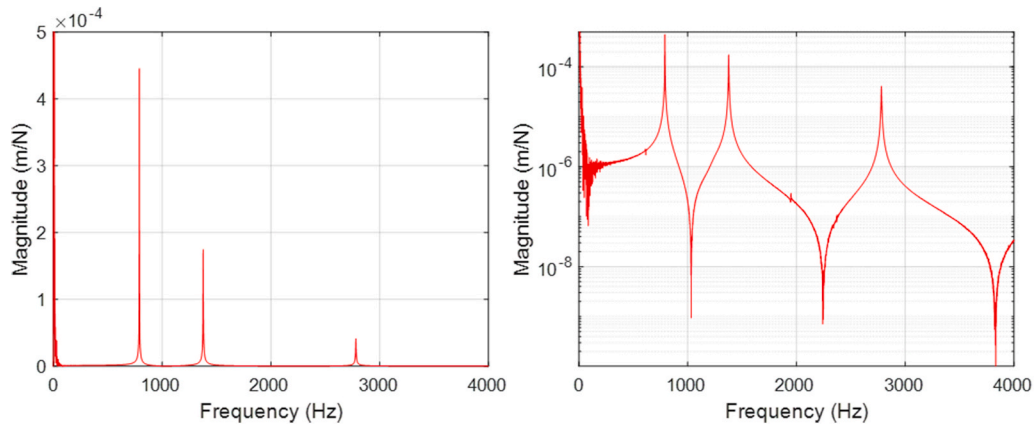


Fig. 7. Direct FRF measurement results for the solid CFFF wall; three CFFF modes are observed at {790.2, 1377.1, and 2780.9} Hz. (Left) Linear magnitude plot. (Right) Semi-logarithmic magnitude plot.

Table 2  
First three wall natural frequencies from finite element analysis.

Model parameter	Value			Value		
	Mode 1	Mode 2	Mode 3	Mode 1	Mode 2	Mode 3
$E$ (Pa)	$2 \times 10^{11}$			$2 \times 10^{11}$		
$g$ (m)	0 (solid)			0.001		
$\rho$ (kg/m <sup>3</sup> )	7700			7700		
$\nu$ (-)	0.3			0.3		
$f_n$ (Hz)	1186	1787	3362	767	1474	2535
Model parameter	Value			Value		
	Mode 1	Mode 2	Mode 3	Mode 1	Mode 2	Mode 3
$E$ (Pa)	$2 \times 10^{11}$			$2 \times 10^{11}$		
$g$ (m)	0.002			0.003		
$\rho$ (kg/m <sup>3</sup> )	7700			7700		
$\nu$ (-)	0.3			0.3		
$f_n$ (Hz)	630	1384	2172	483	1178	1510

internal cut within the solid wall. The cut included three configurations for the {1, 2, and 3} mm core widths. The powder was inserted in the same sketch by extruding a separate body with the powder properties into the vacancy left by the cut. For the CFFF boundary conditions, the wall was fixed along its bottom edge, which represented the (idealized) connection to the wall foundation. The solid wall and powder core were connected using a globally-bonded contact to simulate the core touching

every face of the inside of the wall; the simulation was then executed as a single body.

The parameters in Table 1 were applied, where  $E$  is the solid wall elastic modulus (Pa),  $g$  is the powder core width (m),  $\rho$  is the solid wall density (kg/m<sup>3</sup>),  $\nu$  is Poisson’s ratio (-) for the solid wall, and  $f_n$  is the predicted natural frequency (Hz). The material properties in Table 1 were assumed; no measurements were completed since the intent of the

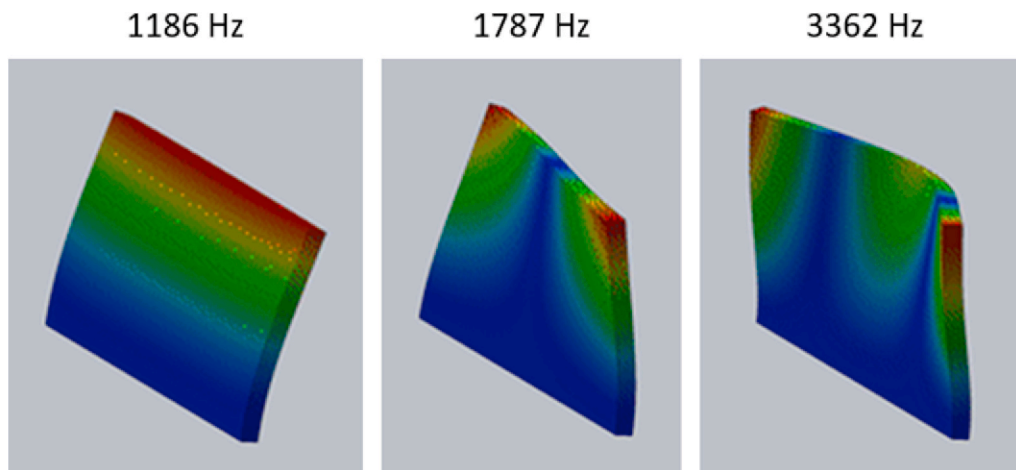


Fig. 8. First three mode shapes and corresponding natural frequencies for the solid wall from finite element analysis. The clamped boundary condition is at the bottom of the wall.

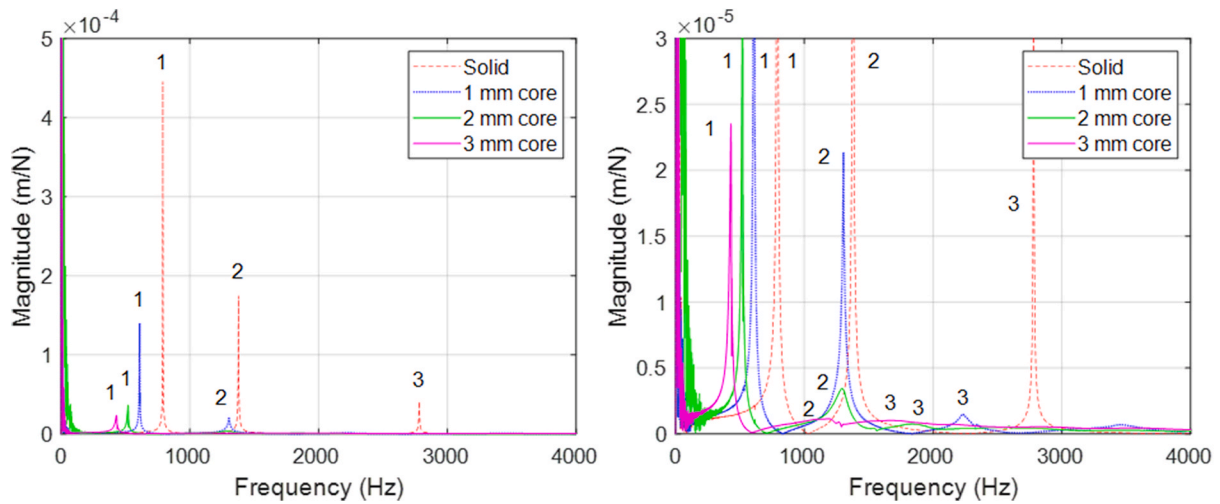


Fig. 9. Direct FRF magnitudes for all four walls. (Left) Full scale. (Right) Magnified scale to view modes with higher dynamic stiffness. The mode numbers are identified as {1, 2, or 3} for each of the four walls.

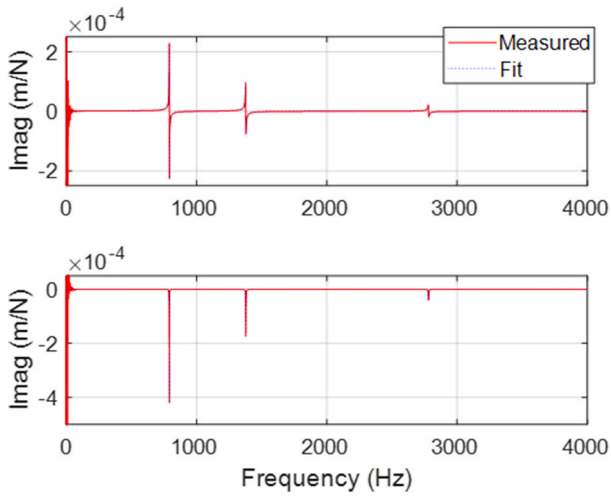


Fig. 10. Measurement and modal fit for solid wall.

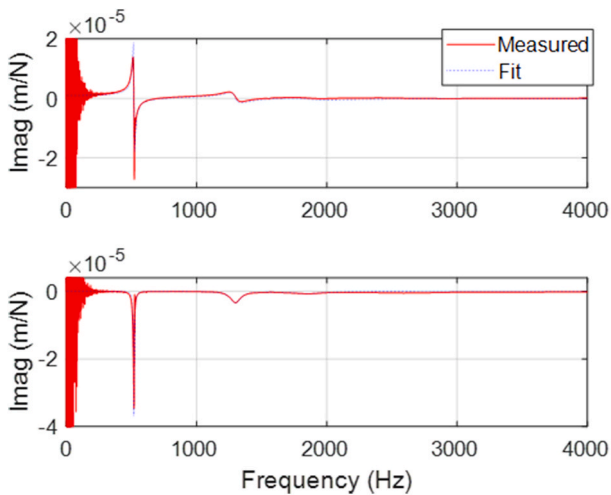


Fig. 11. Measurement and modal fit for 2 mm powder core wall.

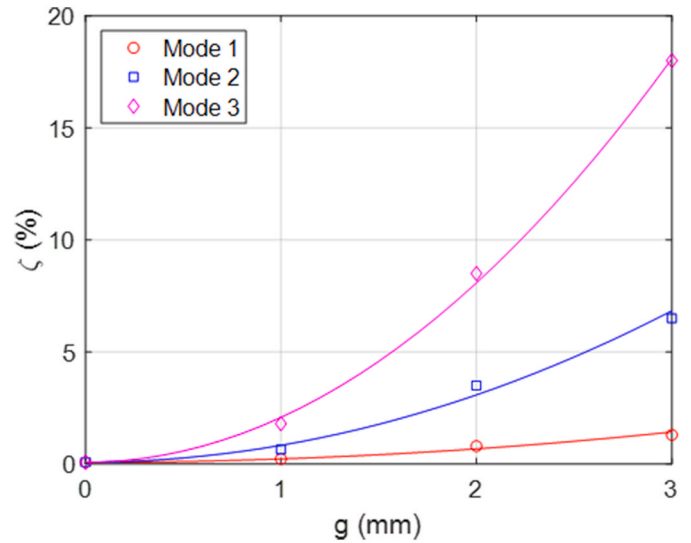


Fig. 12. Variation in damping ratio,  $\zeta$ , with powder core width,  $g$ , and mode number. Both the data (symbols) and second-order fits (lines) are shown.

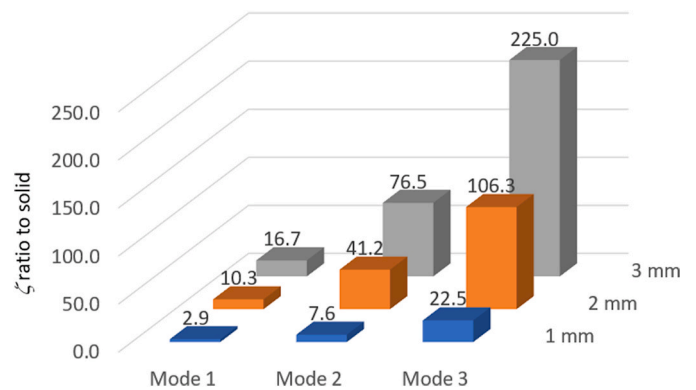


Fig. 13. Change in damping ratio with core width and mode number. The  $\zeta$  value is normalized to the solid  $\zeta$  value for each mode. For example, the 1 mm core first mode  $\zeta$  value is 2.9 times higher than the first mode  $\zeta$  value for the solid wall.

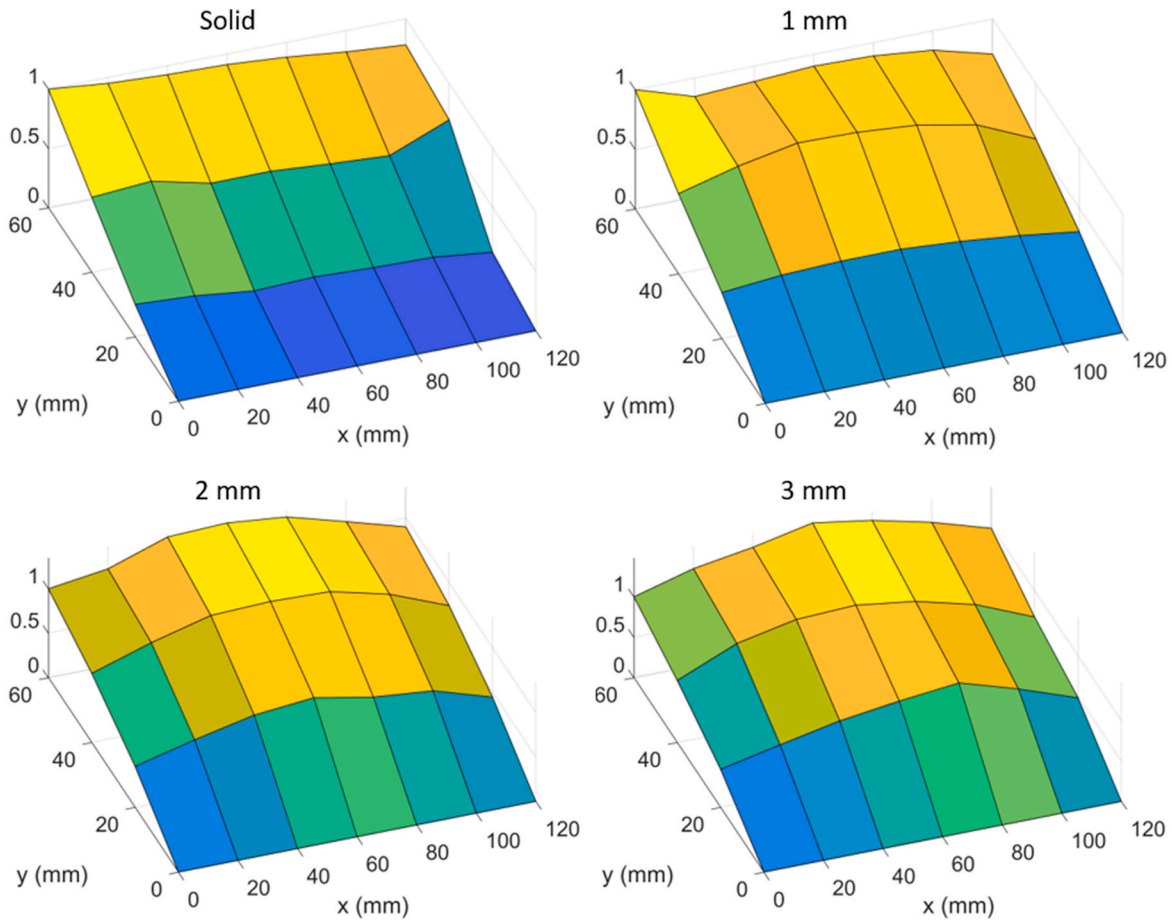


Fig. 14. Measured mode shapes for the first mode from the solid (top left), 1 mm core (top right), 2 mm core (bottom left), and 3 mm core (bottom right) walls.

finite element modeling was simply to guide the wall designs. It was also assumed that the captured powder density was half the sintered metal density ( $3850 \text{ kg/m}^3$ ) and that the powder offered no appreciable resistance to deformation (1 MPa elastic modulus). The results are presented in Table 2. Fig. 8 displays the first three modes shapes for the solid wall geometry. To obtain these results, the simulation mesh size was 1 mm across the 5 mm wall thickness (i.e., there were five layers across the wall). The size was  $0.1 \text{ mm} \times 0.1 \text{ mm}$  for the  $120 \text{ mm} \times 60 \text{ mm}$  wall surface. Convergence was confirmed by decreasing the mesh size across the wall thickness from 5 mm in intervals of 0.25 mm until the largest change in natural frequency for the first three modes was less than 1.5%. This was achieved by the 1 mm mesh size.

#### 4. Results and discussion

Two effects were considered. First, the change in damping ratio for the first three modes was quantified as the powder core width was increased from 0 mm (solid) to 3 mm in 1 mm increments. Second, the change in mode shape geometry for the first three modes was evaluated as the powder core width increased. To quantify the damping increase, Fig. 9 displays the direct FRFs for all four walls. Because not all modes can be viewed at full scale (left); a magnified scale plot is also provided (right). The natural frequencies are labeled as {1, 2, or 3} for each of the four walls. It is seen that as the captured powder volume increases, the damping also increases because the magnitude decreases.

To quantify the change in damping, modal fitting was performed to identify the (viscous) damping ratios,  $\zeta$ , for the first three modes of the four walls. To demonstrate, the measurement and fit for the solid wall are shown in Fig. 10; the three damping ratios are 0.00078, 0.00085, and 0.00080 (or 0.078%, 0.085%, and 0.080%) for the three modes.

This low damping is typical for monolithic, metallic structures. As a second example, the measurement and fit for the 2 mm powder core wall are displayed in Fig. 11; the three damping ratios are 0.008, 0.035, and 0.085 (or 0.8%, 3.5%, and 8.5%). All 12  $\zeta$  values (%) are summarized in Fig. 12; a second-order fit for each mode is also displayed. These fits are described by Eqs. (1)–(3), where  $\zeta_i$  is the fit (%) for mode number  $i = 1, 2$ , and 3 and  $g$  is the powder core width (mm).

$$\zeta_1 = 0.078 + 0.15g^2 \quad (1)$$

$$\zeta_2 = 0.085 + 0.75g^2 \quad (2)$$

$$\zeta_3 = 0.080 + 2.0g^2 \quad (3)$$

Additionally, the ratio of the powder core  $\zeta$  values to the solid wall  $\zeta$  values for each mode are shown in Fig. 13. From Figs. 12 and 13, it is evident that: 1) the captured powder dramatically increases damping for the walls; and 2) the damping increase is mode dependent with higher rates of increase with higher mode number. Presumably, this is because the higher order modes exhibit more complicated deformation geometries and therefore more opportunities for energy dissipation through relative motion within the powder and between the powder and wall internal surfaces.

Next, the modification in mode shape with powder core width (and solid wall thickness) was studied. Experimental results for the first mode shape from the four walls are displayed in Fig. 14. First, it is seen that, while the solid wall mode shape is essentially flat in the  $x$  direction, the powder core mode shapes depart from the flat geometry and show increasing “bowing” in the middle, where the bow tends to move from the free end toward the base as the core width increases. This is related to the change in local wall stiffness. Fig. 14 demonstrates that the

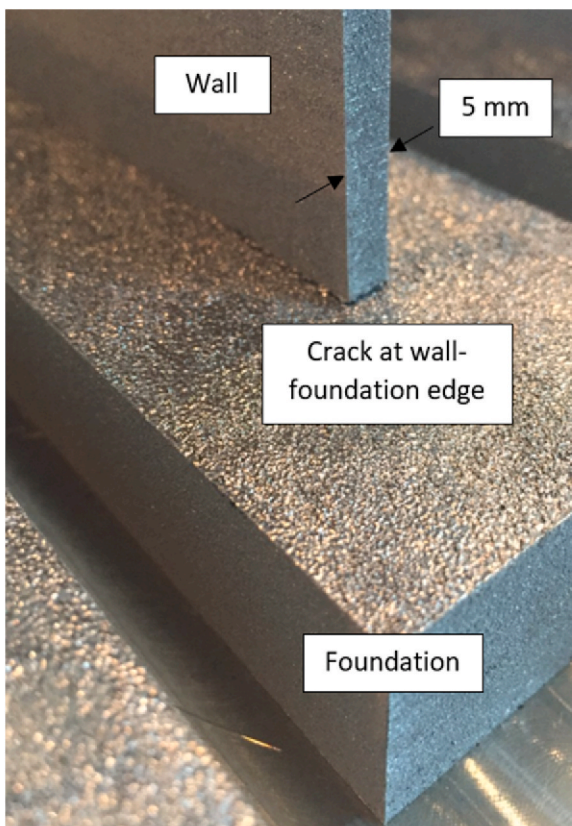


Fig. 15. Crack at clamped boundary condition for the solid wall.

presence of the powder core not only increases damping, but also modifies the mode shape as the solid geometry is changed to accommodate its presence. Second, it is seen that the top left corner, i.e., the  $(x, y) = (0, 60)$  mm location, exhibits increased local amplitude for the solid and 1 mm powder core results. The source of this anomaly is a small crack at the  $(0, 0)$  mm end of the ideally rigid connection between the wall and foundation for both parts; a photograph of the edge crack for the solid wall is shown in Fig. 15 (the crack for the 1 mm core wall was similar, but smaller). The explanation for these local failures is thermal gradients and residual stress that occur during the part build [20]. No cracks were observed for the 2 mm and 3 mm powder core geometries. This suggests a close relationship between thermal deformation, residual stress, and the presence of captured powder.

A similar trend is observed for the third mode. Fig. 16 displays the solid, 1 mm core, and 2 mm core measured mode shapes. The 3 mm core result is not included because the damping was so high that the mode shape was difficult to accurately extract from the direct and cross FRF measurements. Similar to the first mode results presented in Fig. 14, the third mode is increasingly distorted with a larger powder core width (with fixed wall thickness).

To confirm these results, the finite element model mode shapes were also evaluated with increasing powder core width. Similar to Figs. 14 and 16, Figs. 17–19 display the change in mode shape geometry for the first, second, and third modes. To enable comparison with Figs. 14 and 16, the same  $3 \times 7$  grid pattern was applied, although the actual mesh had much higher resolution. Again, mode shape deformation is observed with increasing departure from the solid wall mode shape as the powder core width increases. To directly observe the change in mode shape geometries, difference maps were calculated where the finite element solid wall mode shape was subtracted from the finite element powder core mode shapes. These results are displayed in Figs. 20–22. In each case, the distortion grows and shifts towards the clamped boundary with increasing core width.

Finally, comments on the modeled (finite element analysis) and measured (impact testing) natural frequencies are warranted. Their comparison is shown in Table 3, including the percent difference. It is seen that the modeled values overpredict the measured natural frequencies in 10 of 12 cases. First, a potential source of this disagreement is that wrought stainless steel nominal mechanical properties were assumed in the finite element models. The elastic modulus of the printed material may be less than the assumed value of 200 GPa, for example, which would cause the natural frequencies to be overpredicted. Second, the large change in cross-section at the transition from foundation to wall (50 mm width to 5 mm width) can influence the local microstructure during printing. This could disrupt the idealized clamped boundary condition assumed in the finite element analysis. Third, the three largest percent differences ( $-33.4\%$ ,  $-22.9\%$ , and  $-20.5\%$ ) are for the first two modes of the solid wall and the first mode of the 1 mm core wall. As noted, a crack was observed at the edge of the wall-foundation interface in both cases (see Fig. 15 for the solid wall crack), which would serve to reduce the measured natural frequencies due to the deviation from the assumed clamped boundary condition.

## 5. Conclusions

This paper reported the fabrication, modeling, and impact testing of powder bed printed stainless steel walls with captured powder cores. It was confirmed that increased structural damping and mode shape modification were obtained from the inclusion of the unmelted powder cores within the solid walls. The damping increase was substantial in all cases. For the first mode, factors of {2.9, 10.3, and 16.7} over the solid wall (viscous) damping ratio were recorded for the {1, 2, and 3} mm powder core widths (fixed 5 mm wall width). For the third mode, these factors increased to {22.5, 106.3, and 225}. Fits to the measured damping ratios showed a second-order dependence on the core width.

The mode shapes were measured by impact testing and modeled using finite element analysis. It was observed in both cases that the mode shapes were increasingly distorted from the solid wall result as the core width increased. It is suggested that the increase in mode shape geometric complexity for higher orders is a contributor to the increased damping seen at higher natural frequencies. The mode shape measurements also showed sensitivity to imperfections in the as-built walls. A crack was observed at the edge of the wall-foundation interface for the solid geometry. A smaller crack was seen for the 1 mm core and no cracks were visible for the 2 mm and 3 mm cores. The first mode shapes for both the solid and 1 mm core walls showed a local increase in amplitude at the wall end where the cracks were located. The absence of cracks for the larger core widths suggests a causal relationship between the core width and the distortions/residual stresses caused by large thermal gradients during the printing process.

Finally, a comparison between the measured and modeled natural frequencies was provided. As expected, the natural frequencies decreased in both models and measurements for all modes as the core width increased. This is due to the change in stiffness and mass with cross-section geometry. It was also seen that the finite element models generally overpredicted the natural frequencies relative to the measurements (10 out of 12 cases). This was attributed to: 1) nominal mechanical properties for wrought stainless steel were assumed in the finite element models; 2) the large change in cross-section at the transition from foundation to wall (50 mm width to 5 mm width) can influence the local microstructure during printing and, therefore, the boundary condition, which was idealized as clamped in the finite element models; and 3) the small cracks at the edge of the wall-foundation interface for the solid and 1 mm walls also affect the ideally clamped boundary condition and decrease the measured natural frequencies.

## Declaration of Competing Interest

The authors declare that they have no known competing financial

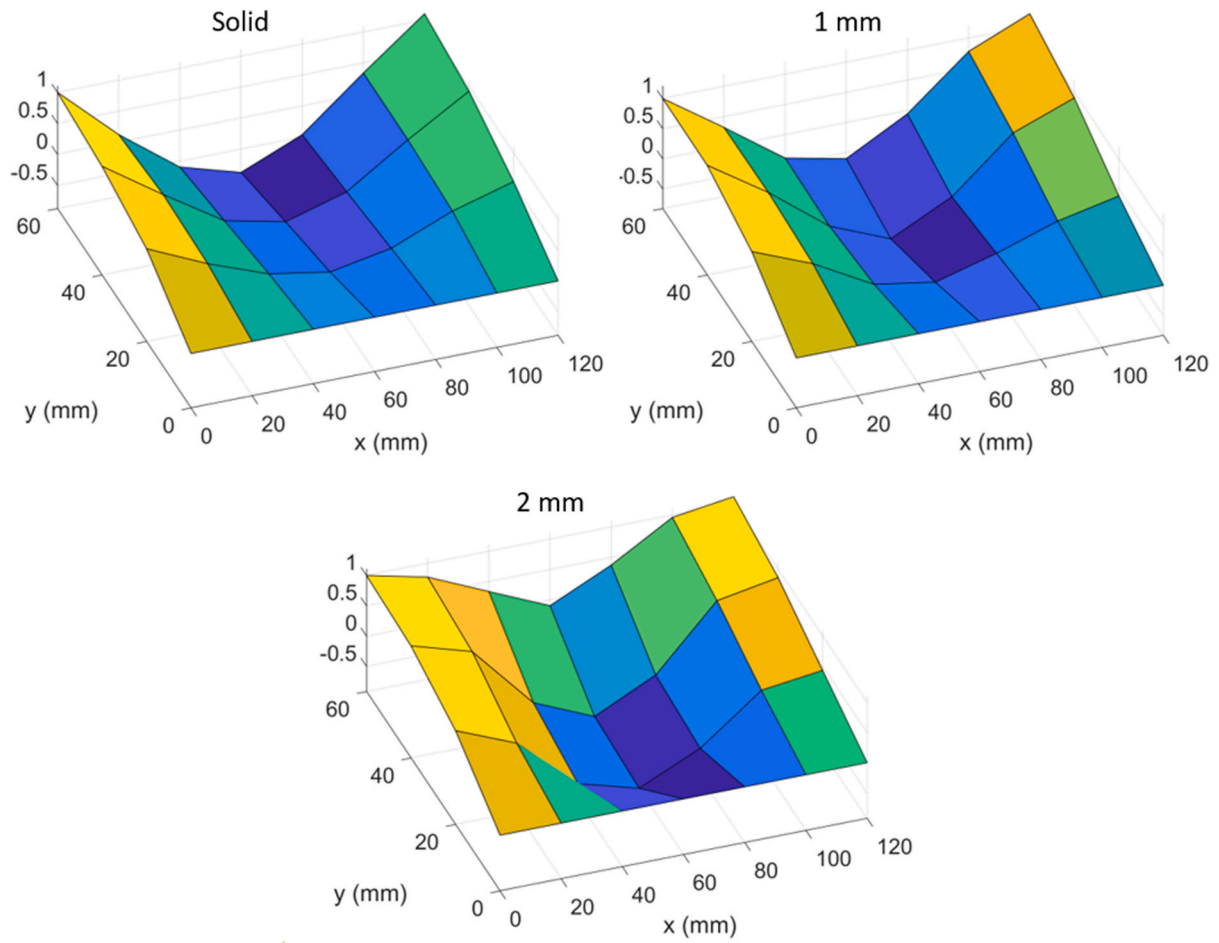


Fig. 16. Measured mode shapes for the third mode from the solid (top left), 1 mm core (top right), and 2 mm core (bottom) walls.

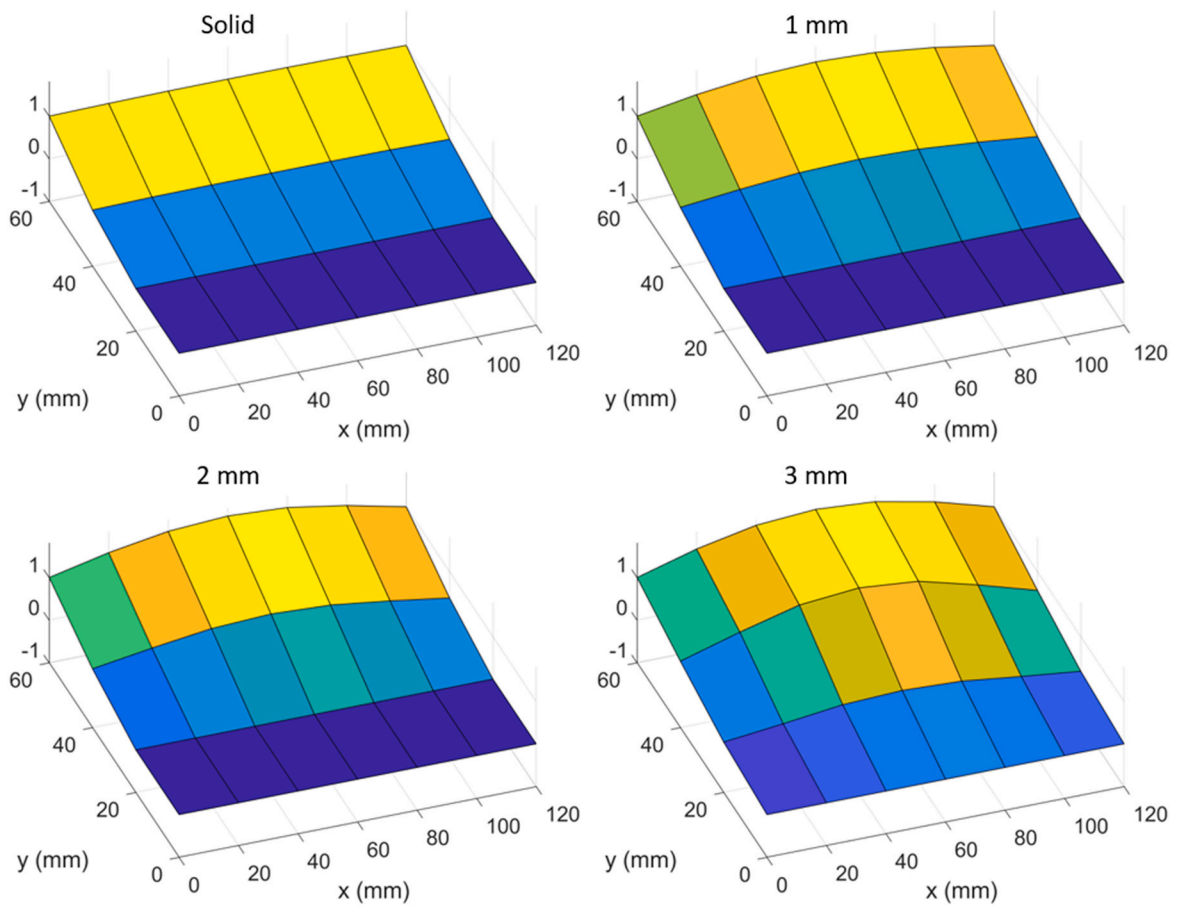


Fig. 17. Modeled mode shapes for the first mode from the solid (top left), 1 mm core (top right), 2 mm core (bottom left), and 3 mm core (bottom right) walls.

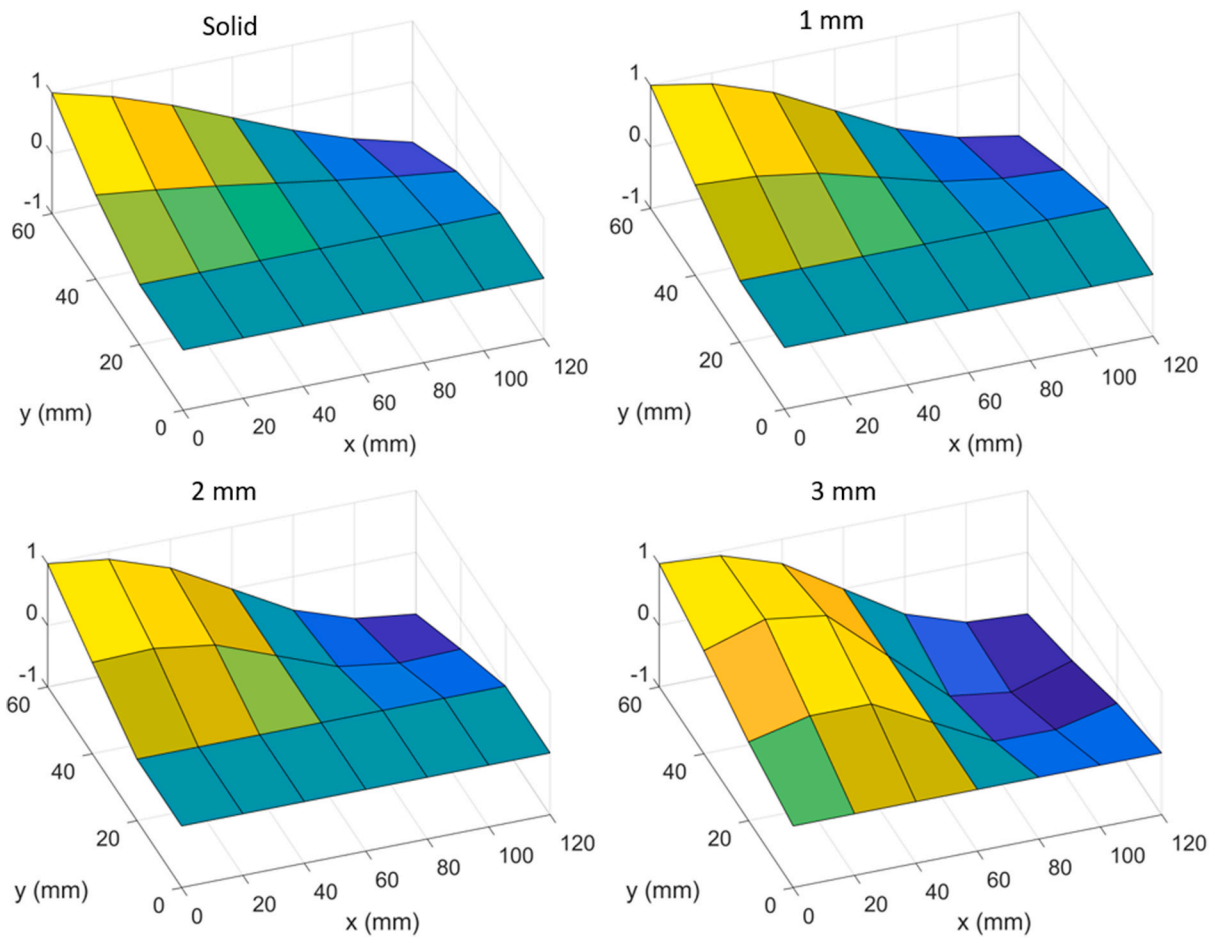


Fig. 18. Modeled mode shapes for the second mode from the solid (top left), 1 mm core (top right), 2 mm core (bottom left), and 3 mm core (bottom right) walls.

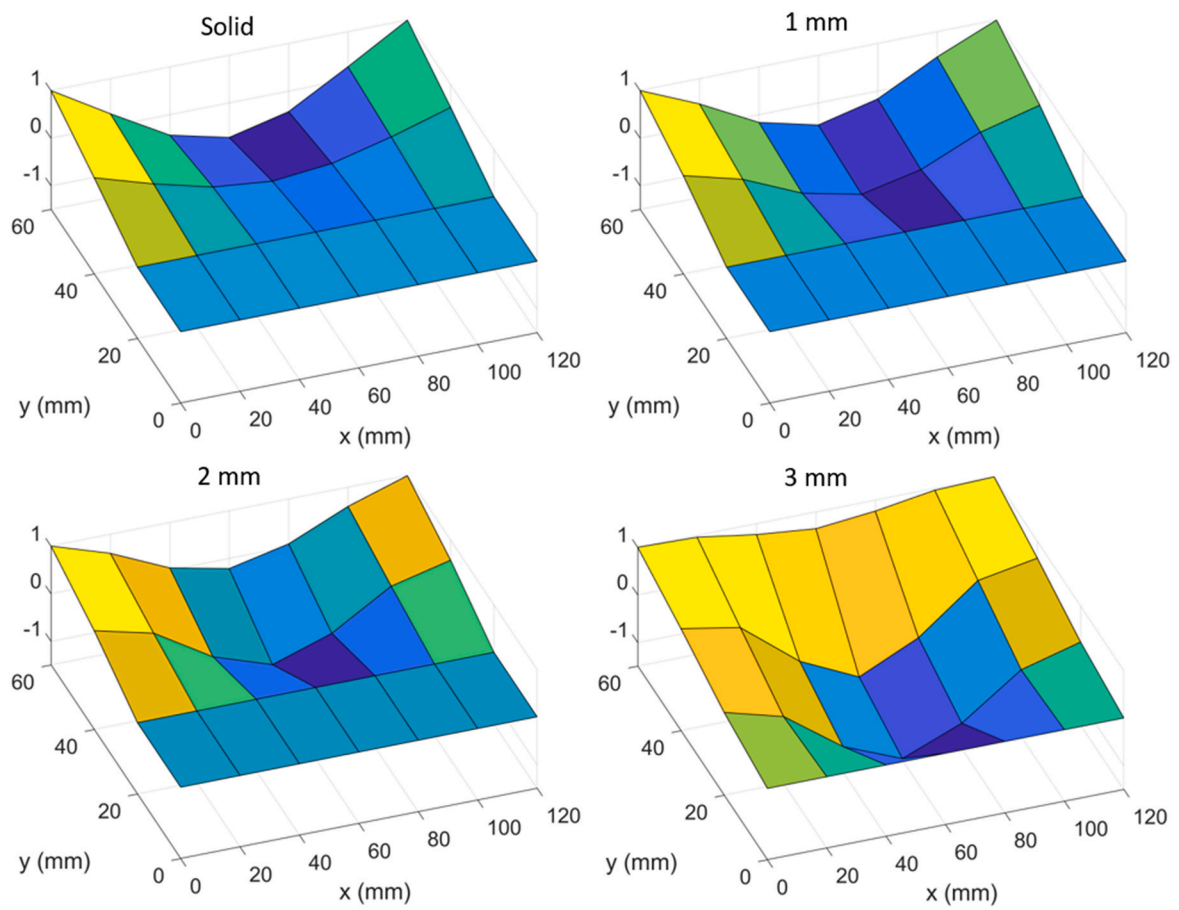
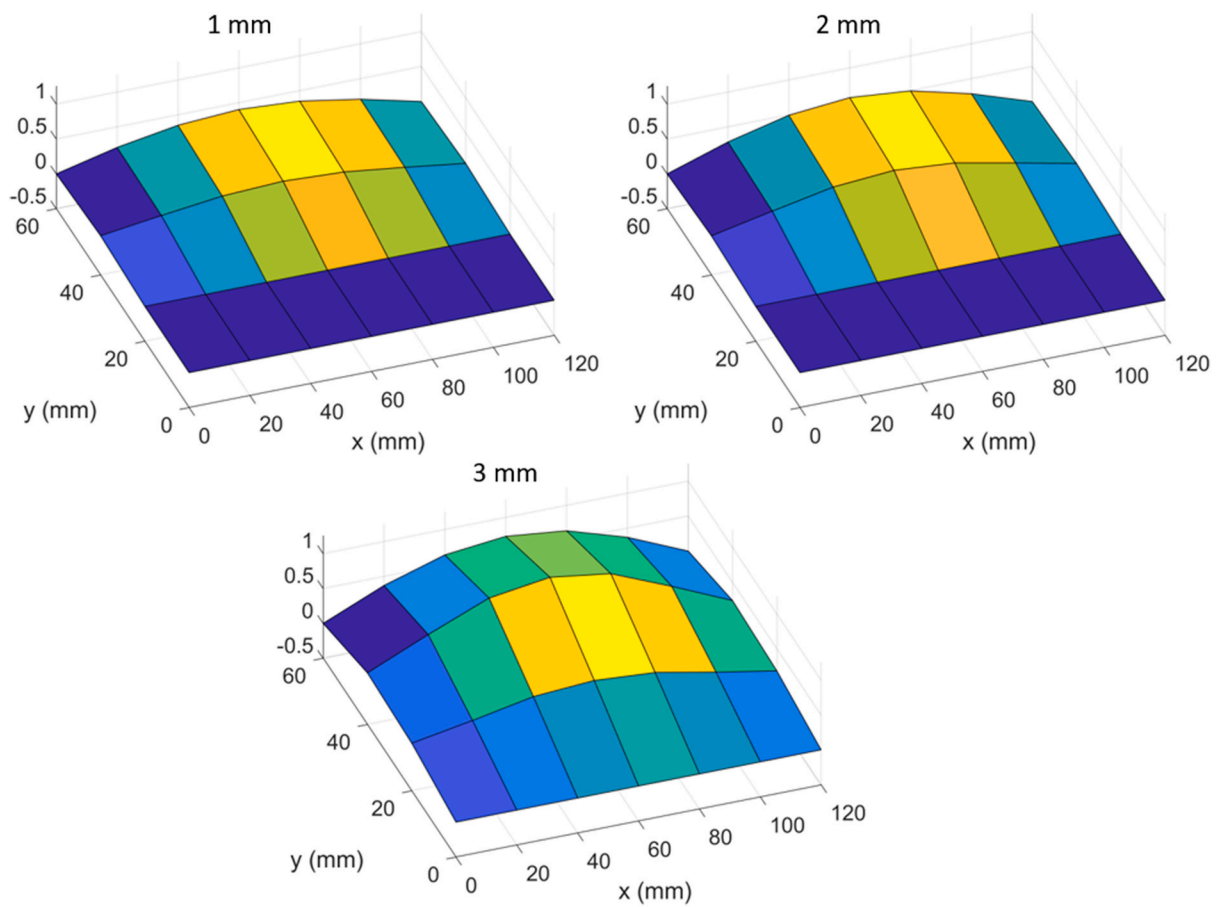
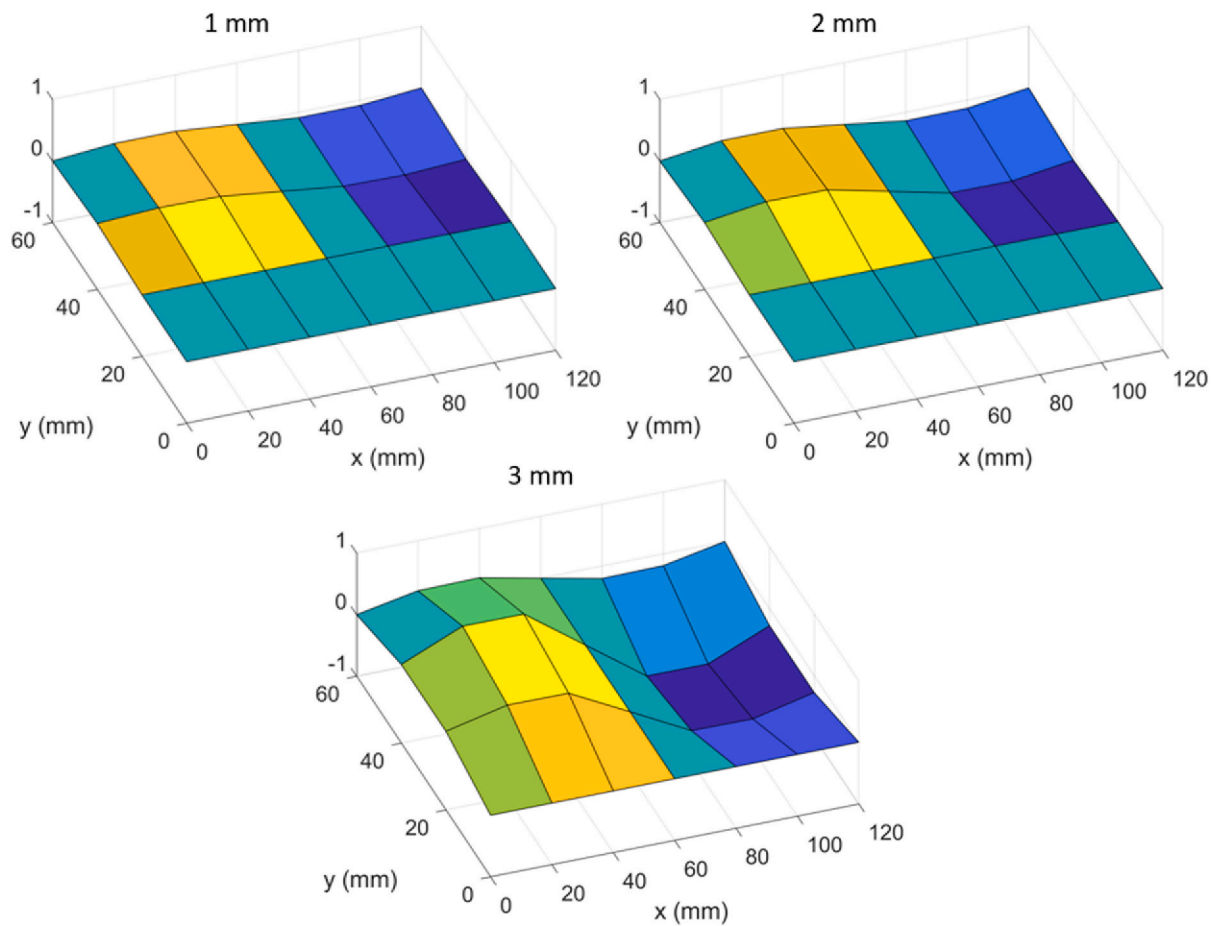


Fig. 19. Modeled mode shapes for the third mode from the solid (top left), 1 mm core (top right), 2 mm core (bottom left), and 3 mm core (bottom right) walls.



**Fig. 20.** Difference maps for modeled first mode shapes. The solid wall first mode result was subtracted from the 1 mm core (top left), 2 mm core (top right), and 3 mm core (bottom) first mode shapes.



**Fig. 21.** Difference maps for modeled second mode shapes. The solid wall second mode result was subtracted from the 1 mm core (top left), 2 mm core (top right), and 3 mm core (bottom) second mode shapes.

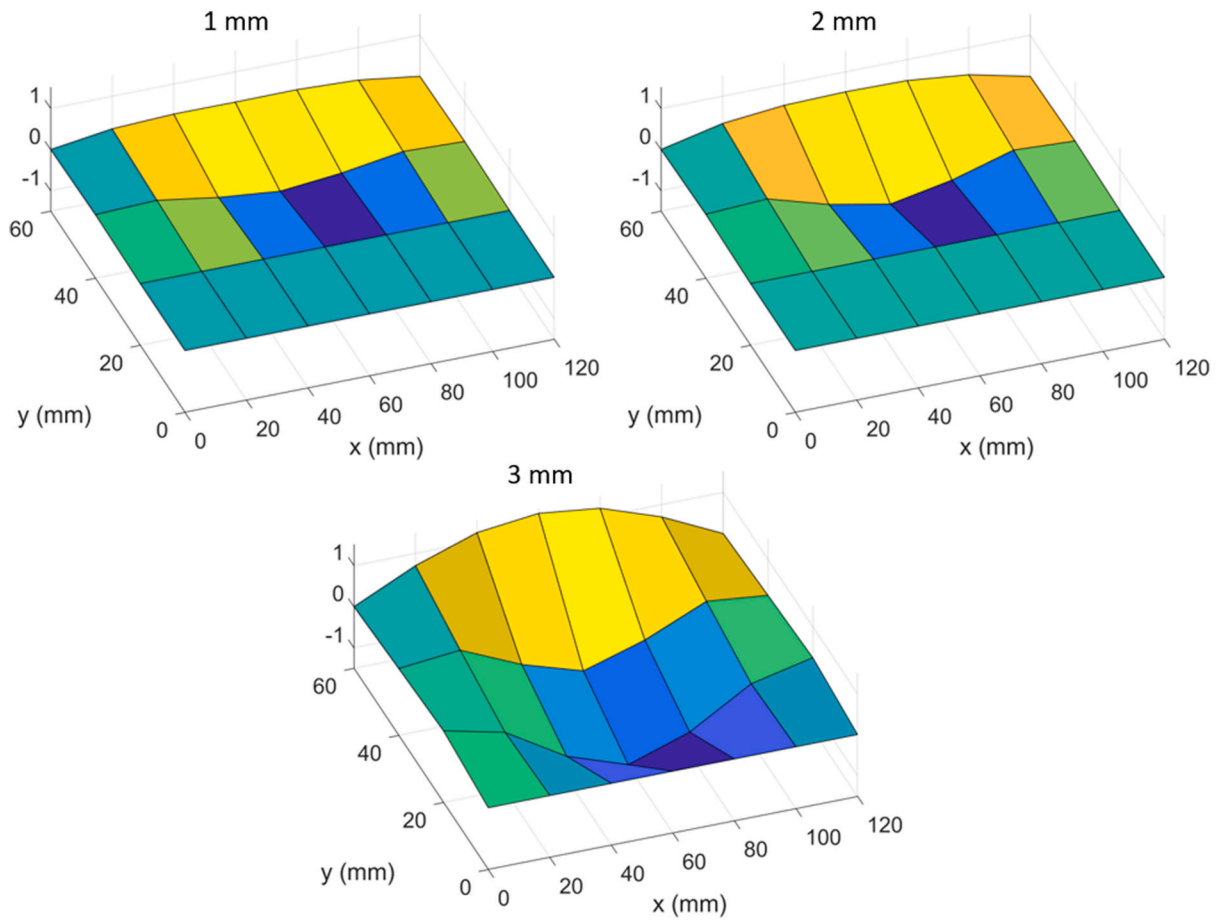


Fig. 22. Difference maps for modeled third mode shapes. The solid wall third mode result was subtracted from the 1 mm core (top left), 2 mm core (top right), and 3 mm core (bottom) third mode shapes.

Table 3  
Finite element and measured natural frequencies.

Core width, g (mm)	Finite element $f_n$ (Hz)			Measured $f_n$ (Hz)			Percent difference (%)		
	Mode 1	Mode 2	Mode 3	Mode 1	Mode 2	Mode 3	Mode 1	Mode 2	Mode 3
0	1186	1787	3362	790	1377	2781	-33.4	-22.9	-17.3
1	767	1474	2535	610	1304	2233	-20.5	-11.5	-11.9
2	630	1384	2172	519	1300	1860	-17.6	-6.1	-14.4
3	483	1178	1510	429	1210	1750	-11.2	2.7	15.9

interests or personal relationships that could have appeared to influence the work reported in this paper.

**Acknowledgements**

This research was supported by the DOE Office of Energy Efficiency and Renewable Energy (EERE), Energy and Transportation Science Division, and used resources at the Manufacturing Demonstration Facility, a DOE-EERE User Facility at Oak Ridge National Laboratory. The authors gratefully acknowledge contributions by E. Betters, ORNL, to the finite element analysis.

**References**

[1] Ngo TD, Kashani A, Imbalzano G, Nguyen KT, Hui D. Additive manufacturing (3D printing): a review of materials, methods, applications and challenges. *Compos B Eng* 2018;143:172–96.  
 [2] Lewandowski JJ, Seifi M. Metal additive manufacturing: a review of mechanical properties. *Annu Rev Mater Res* 2016;46:151–86.

[3] Bikas H, Stavropoulos P, Chryssolouris G. Additive manufacturing methods and modelling approaches: a critical review. *Int J Adv Manuf Technol* 2016;83(1–4): 389–405.  
 [4] Frazier WE. Metal additive manufacturing: a review. *J Mater Eng Perform* 2014;23(6):1917–28.  
 [5] Sames WJ, List FA, Pannala S, Dehoff RR, Babu SS. The metallurgy and processing science of metal additive manufacturing. *Int Mater Rev* 2016;61(5):315–60.  
 [6] Babu SS, Love L, Dehoff R, Peter W, Watkins TR, Pannala S. Additive manufacturing of materials: opportunities and challenges. *MRS Bull* 2015;40(12): 1154–61.  
 [7] Schmitz T, Betters E, West J. Increased damping through captured powder in additive manufacturing. *Manufact Lett* 2020;25:1–5. <https://doi.org/10.1016/j.mfglet.2020.05.003>.  
 [8] Schmitz T, Smith KS. *Mechanical vibrations: modeling and measurement*. Springer Science & Business Media; 2011.  
 [9] Scott-Emuakpor O, George T, Runyon B, Holycross C, Langley B, Sheridan L, O’Hara R, Johnson P, Beck J. June. Investigating damping performance of laser powder bed fused components with unique internal structures. In: *ASME turbo expo 2018: turbomachinery technical conference and exposition*. American Society of Mechanical Engineers Digital Collection; 2018.  
 [10] Scott-Emuakpor OE, George T, Beck J, Runyon BD, O’Hara R, Holycross C, Sheridan L. Inherent damping sustainability study on additively manufactured nickel-based alloys for critical part. In: *AIAA scitech 2019 forum*; 2019. 0410.

- [11] Scott-Emuakpor O, George T, Runyon B, Sheridan L, Holycross C, O'Hara R. June. Assessing manufacturing repeatability of inherently damped nickel alloy components via forced-response testing. Turbo expo: power for land, sea, and air, vol. 58677. American Society of Mechanical Engineers; 2019, V006T24A010.
- [12] Scott-Emuakpor O, George T, Runyon B, Langley B, Sheridan L, Holycross C, O'Hara R, Johnson P. Forced-response verification of the inherent damping in additive manufactured specimens. *Mechanics of additive and advanced manufacturing*, tome 8. Cham: Springer; 2019. p. 81–6.
- [13] Scott-Emuakpor OE, Beck J, Runyon B, George T. Multi-factor model for improving the design of damping in additively manufactured components. In: AIAA scitech 2020 forum; 2020. p. 1631.
- [14] Gagnon L, Morandini M, Ghiringhelli GL. A review of particle damping modeling and testing. *J Sound Vib* 2019;114865.
- [15] Yap CY, Chua CK, Dong ZL, Liu ZH, Zhang DQ, Loh LE, Sing SL. Review of selective laser melting: materials and applications. *Appl Phys Rev* 2015;2(4):041101.
- [16] Wang YM, Voisin T, McKeown JT, Ye J, Calta NP, Li Z, Zeng Z, Zhang Y, Chen W, Roehling TT, Ott RT. Additively manufactured hierarchical stainless steels with high strength and ductility. *Nat Mater* 2018;17(1):63–71.
- [17] Gorsse S, Hutchinson C, Gouné M, Banerjee R. Additive manufacturing of metals: a brief review of the characteristic microstructures and properties of steels, Ti-6Al-4V and high-entropy alloys. *Sci Technol Adv Mater* 2017;18(1):584–610.
- [18] Zhang B, Dembinski L, Coddet C. The study of the laser parameters and environment variables effect on mechanical properties of high compact parts elaborated by selective laser melting 316L powder. *Mater Sci Eng. A* 2013;584: 21–31.
- [19] Liu Y, Yang Y, Mai S, Wang D, Song C. Investigation into spatter behavior during selective laser melting of AISI 316L stainless steel powder. *Mater Des* 2015;87: 797–806.
- [20] Sochalski-Kolbus LM, Payzant EA, Cornwell PA, Watkins TR, Babu SS, Dehoff RR, Lorenz M, Ovchinnikova O, Duty C. Comparison of residual stresses in Inconel 718 simple parts made by electron beam melting and direct laser metal sintering. *Metall Mater Trans* 2015;46(3):1419–32.